ADVANCED MATERIALS
www.advmat.de

Check for updates

Cation-Disorder Engineering Promotes Efficient Charge-Carrier Transport in $AgBiS_2$ Nanocrystal Films

*Marcello Righetto, Yongjie Wang, Karim A. Elmestekawy, Chelsea Q. Xia, Michael B. Johnston, Gerasimos Konstantatos, and Laura M. Herz**

Efficient charge-carrier transport is critical to the success of emergent semiconductors in photovoltaic applications. So far, disorder has been considered detrimental for charge-carrier transport, lowering mobilities, and causing fast recombination. This work demonstrates that, when properly engineered, cation disorder in a multinary chalcogenide semiconductor can considerably enhance the charge-carrier mobility and extend the charge-carrier lifetime. Here, the properties of $AgBiS_2$ nanocrystals (NCs) are explored as a function of Ag and Bi cation-ordering, which can be modified via thermal-annealing. Local Ag-rich and Bi-rich domains formed during hot-injection synthesis are transformed to induce homogeneous disorder (random Ag-Bi distribution). Such cation-disorder engineering results in a sixfold increase in the charge-carrier mobility, reaching ≈2.7 $cm^2 V^{-1} s^{-1}$ in $AgBiS_2$ NC thin films. It is further demonstrated that homogeneous cation disorder reduces charge-carrier localization, a hallmark of charge-carrier transport recently observed in silver-bismuth semiconductors. This work proposes that cation-disorder engineering flattens the disordered electronic landscape, removing tail states that would otherwise exacerbate Anderson localization of small polaronic states. Together, these findings unravel how cation-disorder engineering in multinary semiconductors can enhance the efficiency of renewable energy applications.

1. Introduction

Multinary semiconductors—inorganic and hybrid compounds featuring three or more component elements—recently emerged as a versatile material class in energy research with applications ranging from photovoltaics[1,2] to photocatalysis[3,4] and thermoelectrics.[5,6] Although the increased compositional space yields unprecedented opportunities for materials design,[7] it also enhances the role played by disorder.[8,9] Beyond conventional point defects and grain boundaries, substitutional disorder on cation/anion sublattices (e.g., promoted by antisite defects) becomes prominent in multinary semiconductors.[8–11] This so-called "site disorder" generates essentially isostructural semiconductors with different properties based on the site occupancy.

Cation disorder (henceforth CD) is often regarded as an undesirable, entropically-driven effect, negatively impacting the use of multinary semiconductors for optoelectronic applications.[9,12,13] Most notable examples are disordered kesterites (CZTS)[14–16] and $A^{II}B^{IV}N_2$ semiconductors.[17,18] Here, the formation of low-valence cation clusters (i.e., cation segregation disorder) underlies the poor charge-carrier transport properties of these materials through the formation of localized anion *p* states, thus hampering their use in solar cells.[19,20] However, it has also recently been proposed that careful engineering of site disorder could provide an additional degree of freedom in tuning technologically-relevant properties.[9,13,21] This concept has been spectacularly proven for $AgBiS_2$, where careful engineering of CD has allowed Konstantatos and co-workers to develop record-breaking ultrathin $AgBiS_2$ nanocrystals (NCs) solar cells with efficiencies above 9%.[22] $AgBiS_2$ is an $A^{I}B^{III}Z_2$ semiconductor showing considerable substitutional site disorder at A and B cation sites. Ordered crystalline $AgBiS_2$ phases present an ordered cation distribution: semiconducting matildite shows alternated-cation ordering in the three directions of the unit cell, whereas metallic schapbachite presents alternated Ag-S and Bi-S planes ordering.[23] However, the distribution of Ag(I) and Bi(III) cations at the A and B cation sites can also be disordered, with disorder types ranging from cation segregation disorder (i.e., the formation of local Ag-rich and Bi-rich pockets) to homogeneous cation disorder.[21,22,24]

M. Righetto, K. A. Elmestekawy, C. Q. Xia, M. B. Johnston, L. M. Herz
Department of Physics
University of Oxford
Clarendon Laboratory
Parks Road, Oxford OX1 3PU, UK
E-mail: laura.herz@physics.ox.ac.uk
Y. Wang, G. Konstantatos
ICFO—Institut de Ciencies Fotoniques
The Barcelona Institute of Science and Technology
Castelldefels 08860, Barcelona, Spain
G. Konstantatos
ICREA-Institució Catalana de Recerca i Estudia Avançats
Lluis Companys 23, Barcelona 08010, Spain
L. M. Herz
Institute for Advanced Study
Technical University of Munich
Lichtenbergstrasse 2a, D-85748 Garching, Germany
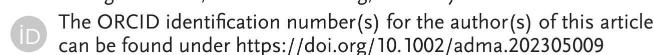
The ORCID identification number(s) for the author(s) of this article can be found under https://doi.org/10.1002/adma.202305009

© 2023 The Authors. Advanced Materials published by Wiley-VCH GmbH. This is an open access article under the terms of the Creative Commons Attribution License, which permits use, distribution and reproduction in any medium, provided the original work is properly cited.

DOI: 10.1002/adma.202305009

© 2023 The Authors. Advanced Materials published by Wiley-VCH GmbH

We define here homogeneous cation disorder as the random distribution of cations across the sublattice (i.e., 50% occupation probability for both Ag and Bi on any cation site), which in $AgBiS_2$ was shown to introduce intermediate electronic states between matildite and schapbachite.[21] In their recent work, Konstantatos and co-workers demonstrated that the transition from a cation-segregated phase to a homogeneous cation-disordered phase significantly enhances the absorption coefficient of $AgBiS_2$ NCs, achieving among the highest absorption coefficients for materials used in photovoltaics.[20,22] This effect is promoted by the increasingly homogeneous distribution of Ag(I) and Bi(III) cations, which results in enhanced spatial delocalization of the electronic bands near the band edges (i.e., a more delocalized density of states, DOS, and thus a higher electronic dimensionality).[21,22,25]

Although CD engineering has emerged as a promising strategy to tune the bandgap and enhance the absorption coefficient in $AgBiS_2$ semiconductors,[21,22] its effects on charge-carrier transport are yet to be explored. Investigating the role of CD on charge-carrier transport in $AgBiS_2$ is even more important in light of recent discoveries about the strong electron–phonon coupling in silver-bismuth semiconductors.[26] Recent works have shown that charge-carrier transport in this emerging family of materials, including $Cs_2AgBiBr_6$,[27,28] Cu_2AgBiI_6,[29] and $Cu_{4x}(AgBi)_{1-x}I_4$,[30] is heavily affected by an ultrafast charge-carrier localization process, which poses an intrinsic limit to photovoltaic performances of these materials.[27] A strong acoustic deformation potential interaction[28] and low structural and electronic dimensionality[29,30] have been proposed as contributing factors promoting localization. Therefore, investigating the effect on charge-carrier transport of strategies modulating these factors, such as CD engineering in $AgBiS_2$ NCs,[21,22] is of the utmost importance for developing efficient Ag-Bi photovoltaic applications.

In this work, we uncover the interplay between ultrafast charge-carrier localization and cation disorder in determining charge-carrier transport in $AgBiS_2$ NC thin films. Here, cation disorder engineering emerges as a powerful strategy to mitigate the deleterious effects of charge-carrier localization in multinary silver-bismuth semiconductors, thus boosting charge-carrier transport.

We study a series of $AgBiS_2$ NC thin films with an engineered degree of CD obtained through mild thermal annealing. The effect of CD on the electronic structure and landscape is investigated using reflection/transmission spectroscopy. Furthermore, the nature of the absorbing states is uncovered by means of low-temperature absorption spectroscopy. After demonstrating the presence of charge-carrier localization in $AgBiS_2$ NCs by using room-temperature and cryogenic optical-pump-terahertz-probe (OPTP) spectroscopy, we reveal for the first time the interaction between this process and CD. We observe that increasingly homogeneous CD (i.e., more random placement of Ag(I) and Bi(III) across the cation sublattice) and therefore increased electronic dimensionality strongly suppresses ultrafast charge-carrier localization and the associated drop in mobility. While such localization is not entirely suppressed, the charge-carrier mobility retained in the localized state is dramatically increased with increasingly homogeneous CD, as a result of the flatter electronic landscape. Altogether, this work demonstrates the possibility of leveraging disorder-engineering to tune the electronic landscape and enhance charge-carrier mobilities in multinary semiconductors. We anticipate this approach to form a leading strategy toward improved performance of multinary silver-bismuth semiconductors in optoelectronic applications.

2. Results and Discussion

Herein, we focus on cation disorder in ternary $AgBiS_2$ nanocrystal (NC) thin films, an emerging environmentally-friendly nanomaterial that has shown promising photovoltaic performance.[22,31–33] In this material, CD can be engineered by overcoming the low (≈20 meV) order–disorder transition barrier through mild thermal annealing and inducing the formation of homogeneous CD.[22] Similar to other ABZ_2 semiconductors,[20,34] as-synthesized $AgBiS_2$ NCs present cation segregation disorder, i.e., the formation of local Ag-rich and Bi-rich domains (**Figure 1**a) within the cubic rock salt structure, as an inevitable consequence of the crystal growth kinetics during the hot-injection synthesis.[22] Here, the formation of homogeneous CD yields isostructural systems that can be interpreted as middle states between the semiconducting cation-ordered phase—see Figure 1a, matildite ($\mathbf{P\bar{3}m1}$)— and the metallic cation-ordered phase schapbachite.[21,25] With increasing thermal annealing temperatures (up to 150 °C), the absorption coefficient of the NC thin films—reported in Figure 1b—shows a dramatic enhancement and significantly redshifts. We note that the as-prepared (unannealed) $AgBiS_2$ NC films already exhibit high crystallinity, as demonstrated previously by high-resolution electron microscopy (see Experimental Section in the Supporting Information),[22] and thermal annealing may therefore not induce the enhancement in crystalline order typically observed for many polycrystalline thin-film light-absorber layers. As such, the changes observed in X-ray diffraction patterns (Figure S1, Supporting Information) have instead recently been shown to reflect an evolution in the ordering of the cation sublattice with annealing temperature.[22] Similarly, observed changes in the absorption coefficient provide evidence for the introduction of homogeneous CD with increasing annealing temperature, yielding a more spatially-delocalized DOS, and forming schapbachite-like states in the bandgap.[21,22] However, less is known about the relation between homogeneous CD and electronic disorder (i.e., inhomogeneous broadening of the absorption tail), which is fundamental for charge-carrier transport in these materials.

2.1. Electronic Landscape of $AgBiS_2$ NC Thin Films

Although the absorption onset contains information about the electronic disorder, there are possible overlapping contributions arising from homogeneous broadening, e.g., from excitonic states. We ruled out any significant presence of excitonic contributions by measuring the absorption coefficient as a function of temperature in the range of 30–295 K (Figure 1c). The absence of clear excitonic peaks at cryogenic temperatures, where such effects would typically be enhanced,[35] confirms that absorption tails observed for $AgBiS_2$ NC thin films instead mostly originate from inhomogeneous broadening (i.e., an electronically-disordered landscape). We modeled the absorption tails using the

© 2023 The Authors. Advanced Materials published by Wiley-VCH GmbH

15214095, 2023, 48, Downloaded from https://onlinelibrary.wiley.com/doi/10.1002/adma.202305009 by Test, Wiley Online Library on [12/12/2023]. See the Terms and Conditions (https://onlinelibrary.wiley.com/terms-and-conditions) on Wiley Online Library for rules of use; OA articles are governed by the applicable Creative Commons License

15214095, 2023, 48, Downloaded from https://onlinelibrary.wiley.com/doi/10.1002/adma.202305009 by Test, Wiley Online Library on [12/12/2023]. See the Terms and Conditions (https://onlinelibrary.wiley.com/terms-and-conditions) on Wiley Online Library for rules of use; OA articles are governed by the applicable Creative Commons License

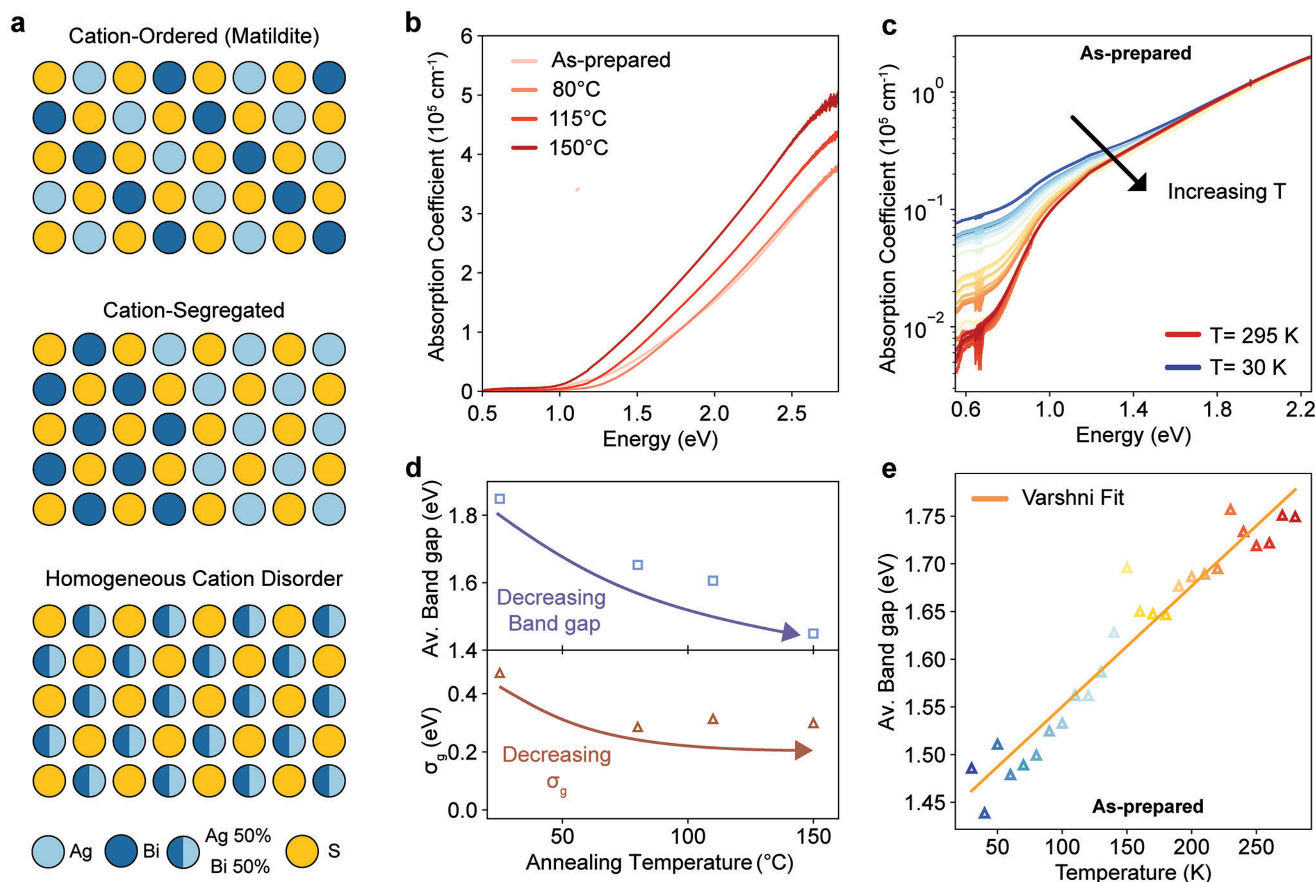

Figure 1. Cation-disorder engineering in $AgBiS_2$ NC thin films. a) Schematic of $AgBiS_2$ crystal structures with different types of cation ordering. Top views of $AgBiS_2$ (001) planes in a cubic rocksalt supercell. The partial occupancy of the Ag^+, Bi^{3+} cation sites is represented as fractional filling of the circles at each site. Top: Matildite (**P$\bar{3}$m1**), middle: cation-segregated and bottom: fully homogeneous cation-disordered (**Fm$\bar{3}$m**) structures. These schematics of $AgBiS_2$ structures depict the ideal ordered, segregated, and homogeneously disordered cases, without accounting for minor statistical fluctuations of the Ag/Bi arrangements that we expect to occur in real materials. b) Absorption coefficient of $AgBiS_2$ NC thin films for films prepared with different thermal annealing temperatures. Two absorption spectra – measured using an InSb detector for energies below 1.22 eV, and Si detector for energies above 1.22 eV – are stitched to generate the reported curves. c) Temperature-dependent absorption coefficient for as-prepared $AgBiS_2$ NC thin films measured between 30 and 295 K. d) Average bandgap ($E_{g,m,}$ blue) and Gaussian distribution (σ_g, brown) as a function of $AgBiS_2$ NC thin-film annealing temperature, obtained by fitting the absorption coefficient shown in (a) to Equation (1). e) Temperature dependence of the average bandgap for as-prepared $AgBiS_2$ NC thin films. The orange line represents a fit to the Varshni model (see Note S2, Supporting Information).

bandgap fluctuation model[15] to quantify this electronic disorder and disentangle it from effects arising from bandgap shifts (Note S1, Supporting Information). In this model, the electronic bandgap E_g turns into a probability distribution function defined by a Gaussian with mean $E_{g,m}$ and width σ_g. While alternative distributions of tail states (e.g., exponential)[36,37] have been proposed for disordered materials, we note that a Gaussian distribution of tail states was found to describe well a range of other disordered materials (e.g., kesterites, CIGS semiconductors).[14,15,38] For direct transitions, the resulting absorption coefficient can be written as

$$\alpha \propto \int_0^\infty \frac{\sqrt{\hbar\omega - E_g}}{\hbar\omega} G\left(E_g\right)\, dE_g \tag{1}$$

where $\hbar\omega$ is the photon energy, and G is a Gaussian function. As shown in Figure S2 (Supporting Information), the bandgap fluctuation model accurately describes the experimental absorption coefficient in the 0.9–1.8 eV photon energy range for all the $AgBiS_2$ NC thin films studied. Notably, increasing thermal annealing temperatures result in a gradual narrowing of the average bandgap from ≈1.84 to ≈1.45 eV (Figure 1d). We note that average bandgaps ($E_{g,m}$), extracted from bandgap fluctuation model fits, and bandgaps (E_g) from literature, extracted by other methods (e.g., Tauc method) or estimated by first principle calculations (e.g., E_g ≈1.55 eV for Matildide-phase $AgBiS_2$[23]), cannot be directly compared because of their different definitions. We expect $E_{g,m}$ to exceed literature-derived E_g, because it accounts for the presence of the Gaussian broadening near the absorption onset.

The observed narrowing of $E_{g,m}$ for annealing at higher temperatures has been predicted[21] and previously observed for $AgBiS_2$ NCs,[22] and results from the formation of schapbachite-like states induced by homogeneous CD. Interestingly, the average bandgap for both as-deposited and 150 °C-annealed thin films is also observed to narrow at lower measurement

© 2023 The Authors. Advanced Materials published by Wiley-VCH GmbH

temperatures (Figure 1e; and Figure S3 and Note S2, Supporting Information), i.e., showing a positive $dE_{g,m}/dT$ and hence a negative value of α of ≈−1.2 meV K^{-1} for as-deposited thin films and −0.5 meV K^{-1} for 150 °C-annealed thin films, associated with fits to the empirical Varshni model reported in Figure 1e; and Figure S3b (Supporting Information) (see Table S1 for all extracted Varshni parameters, Supporting Information). Although similar values were reported for kesterites (CZTS) and Bi_2S_3 (α ≈ 1 and 0.7 meV K^{-1}, respectively),[39,40] the sign of this empirical coefficient is opposite to what is conventionally observed for semiconductors. The presence of an "inverse Varshni effect" (i.e., a negative α value) has been previously reported for lead chalcogenides,[41,42] $AgGaS_2$[43] and other transition metal chalcopyrites, and most notably for lead halide perovskites,[44] but is still poorly understood. It is well-established that the negative dE_g/dT (hence positive Varshni α coefficient) generally observed for conventional semiconductors can be mainly explained in terms of electron–phonon interactions, with the dilation of the lattice playing only a side role.[44] On the other hand, phonon anharmonicity, multiple phonon components and the presence of specific phonon modes that increase the bandgap rather than reduce it have all been indicated as possible causes of the inverse Varshni effect.[45–47] Although phonon anharmonicity has been widely reported for $AgBiS_2$,[24] we note that phonon anharmonicity could only lead to positive dE_g/dT if the band edges showed antibonding characters,[44,48] which has not been reported for $AgBiS_2$.

Importantly, the thermal annealing of the $AgBiS_2$ also yields reduced band tailing – see Figure 1d – with inhomogeneous broadening decreasing gradually with annealing temperature from ≈0.48 for as-prepared films, to ≈0.3 eV for films annealed at 150 °C. Values were extracted from the bandgap fluctuation model described above, and we obtained similar conclusions by applying a standard Urbach method (Figure S4, Supporting Information). Notably, the observed decrease in inhomogeneous broadening with increasing annealing temperatures strongly indicates a more ordered electronic landscape. This effect originates from differences in the DOS associated with cation-segregated and homogeneous CD configurations and is correlated with the observed bandgap shift. As recently demonstrated, homogeneous CD is associated with a more spatially-delocalized DOS, yielding an enhanced absorption coefficient, whereas cation-segregation disorder results in a localized DOS and lower absorption coefficients.[22] Therefore, our analysis confirms that the thermally-induced order–disorder transition in $AgBiS_2$ NCs reshapes the electronic landscape in this material by transforming the weakly absorbing, spatially-localized cation-segregated states (contributing to the absorption tail) into highly absorbing and delocalized states that also cause a bandgap redshift.

2.2. Charge-Carrier Transport in $AgBiS_2$ NC Thin Films

To elucidate the relation between the reshaped electronic landscape and charge-carrier transport in $AgBiS_2$ NC films, we used OPTP spectroscopy. In this technique, changes to the fractional transmission (ΔT/T) of THz pulses, induced by 3.1 eV photoexcitation pulses, allow monitoring of the photoconductivity $\Delta\sigma$ of a material with subpicosecond time resolution. OPTP measurements shown in **Figure 2**a reveal a substantial increase in the photoconductivity signal for $AgBiS_2$ NC thin films as the annealing temperature is increased. To quantitatively compare different thin films, we extract the effective sum mobilities μ_i of photoexcited electrons and holes by converting the sheet photoconductivity measured at the point immediately following photoexcitation, as described in Note S3 and shown in Figure S6 (Supporting Information). Extracted mobility values report a remarkable increase from $\mu_i = 0.46 \pm 0.05\,cm^2\,V^{-1}\,s^{-1}$ for as-prepared thin films to $\mu_i = 2.70 \pm 0.10\,cm^2\,V^{-1}\,s^{-1}$ for 150 °C-annealed thin films. We note that such increases in charge-carrier mobility with increasing annealing temperature do not derive from improved crystallinity, given that detailed XRD and high-resolution transmission electron microscopy investigations on such NC films[22] have revealed that the as-prepared NC films are already highly crystalline (see also Experimental Section). The photoconductivity spectra, recorded at the photoconductivity maximum, are mostly representative of free charge-carrier conductivity[49] (Figure S6a–d, Supporting Information) and show negligible contributions from phonons. However, we observe increasing deviations from such ideal Drude behavior for NC films subjected to higher annealing temperatures. As-prepared films exhibit photoconductivity spectra close to the ideal Drude behaviour (i.e., a flat real part and zero imaginary part of the photoconductivity), as shown in Figure S7a (Supporting Information), whereas thin films annealed at 150 °C diverge from these trends (Figure 2b). Deviations from the ideal Drude behavior are quantified by the Drude–Smith model (see the Supporting Information for details) through a phenomenological backscattering coefficient c, and fits to these curves yield $c \approx -0.11$ and −0.72 for as-prepared films and those annealed at 150 °C, respectively. We assign these deviations from the ideal Drude behavior of photoconductivity to the backscattering of charge carriers from nanocrystal boundaries, which becomes more significant owing to the enhancement of their mobilities in NCs annealed to induce homogeneous CD. Similar backscattering effects have been observed by Motti et al. for $CsPbBr_3$ NCs, and suggest an intra-nanocrystal origin of the measured OPTP photoconductivity.[50]

Here, we note that the effect of Ag/Bi cation disorder in $AgBiS_2$ starkly differs from what has previously been reported for Cu/Zn disorder in CZTS kesterites[51,52] and Cu/Sn disorder in Cu_2SnS_3,[53] where no significant effect of cation disorder on charge-carrier transport was found. Since the mobility values we determine here are extracted at very early times before any charge-carrier recombination has occurred, they must be directly related to the electronic band structure. We therefore conclude that the observed mobility increase must originate from the peculiar contributions of Ag and Bi to the band structure. Similar to the case of other emerging Ag-Bi semiconductors,[27,54] Ag-S orbitals in $AgBiS_2$ NCs mainly contribute to the valence band, whereas Bi-S orbitals contribute primarily to the conduction band, thus inducing a spatial separation of these two electronic bands and a lower electronic dimensionality, in particular if Ag and Bi form segregated domains in the material.[54,55] Therefore, homogeneous CD yields a more spatially-delocalized DOS and a higher electronic dimensionality, which we show here to be associated with higher charge-carrier mobilities and improved transport.[54]

© 2023 The Authors. Advanced Materials published by Wiley-VCH GmbH

15214095, 2023, 48, Downloaded from https://onlinelibrary.wiley.com/doi/10.1002/adma.202305009 by Test, Wiley Online Library on [12/12/2023]. See the Terms and Conditions (https://onlinelibrary.wiley.com/terms-and-conditions) on Wiley Online Library for rules of use; OA articles are governed by the applicable Creative Commons License

15214095, 2023, 48, Downloaded from https://onlinelibrary.wiley.com/doi/10.1002/adma.202305009 by Test, Wiley Online Library on [12/12/2023]. See the Terms and Conditions (https://onlinelibrary.wiley.com/terms-and-conditions) on Wiley Online Library for rules of use; OA articles are governed by the applicable Creative Commons License

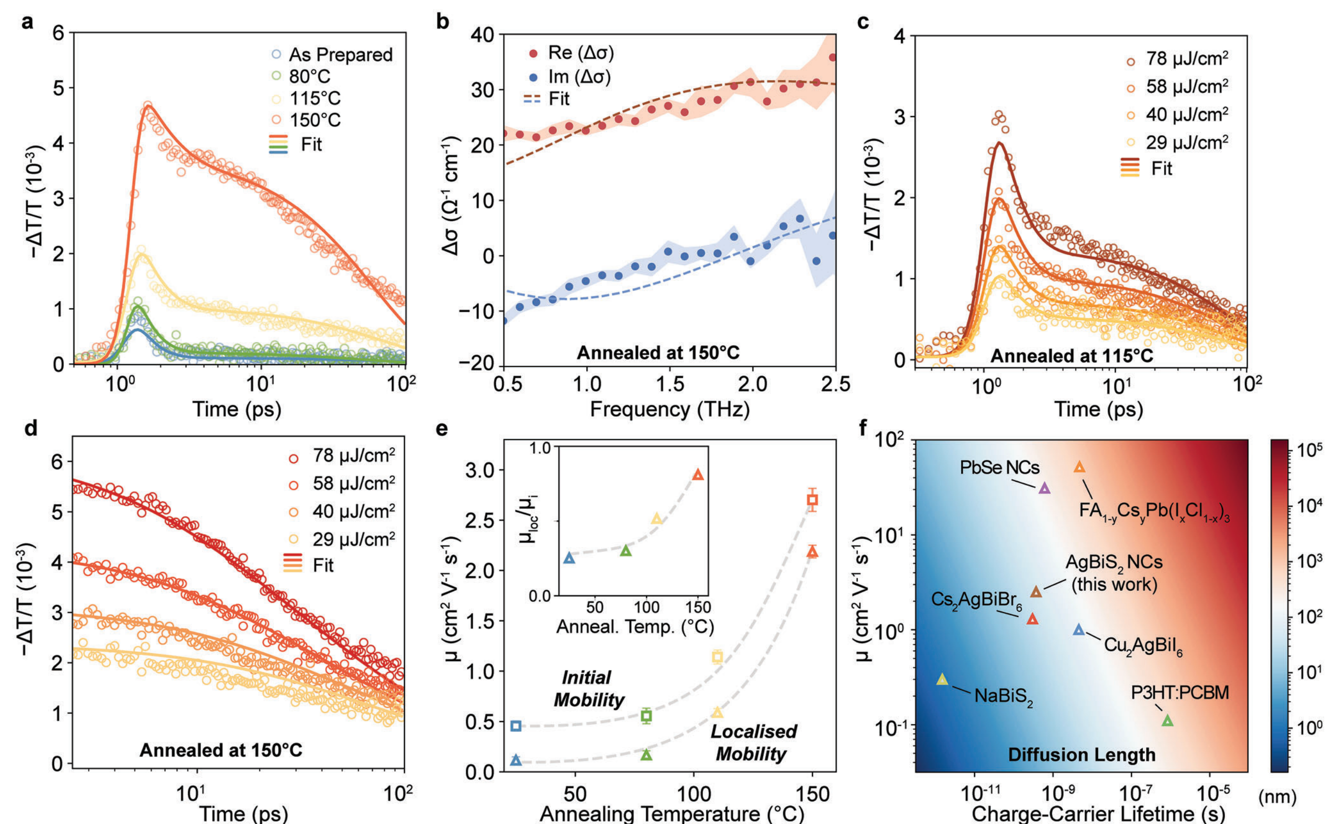

Figure 2. Impact of cation disorder in $AgBiS_2$ NCs on charge-carrier transport. a) Photoinduced THz conductivity for as-deposited (blue), 80 °C-annealed (green), 115 °C-annealed (yellow), and 150 °C-annealed (orange) thin films of $AgBiS_2$ NCs after 3.1 eV pulsed excitation at a fluence of 58 μJ cm^{-2}. Open circles are experimental data, and solid lines represent fits to the two-level mobility model described in the Note S4 (Supporting Information) (Equation (S9) convoluted with a Gaussian instrumental response function, Supporting Information). b) Real (red) and imaginary (blue) part of the photoinduced THz conductivity spectra for $AgBiS_2$ NC thin films annealed at 150 °C, measured at the photoconductivity maximum (t = 1.5 ps) following 3.1 eV excitation at a fluence of 78 μJ cm^{-2}. Dots represent experimental data (with shaded areas indicating statistical error), whereas dashed lines are fits according to the Drude–Smith model (see the Supporting Information). We note that charge-carrier mobilities quoted in the text are derived directly from the sheet photoconductivity (see Note S3, Supporting Information) rather than these Drude–Smith fits. c) Fluence-dependent photoconductivity transients for $AgBiS_2$ NC thin films annealed at 115 °C, measured after 3.1 eV pulsed excitation with a range of different excitation fluences. Open circles are experimental data and solid lines represent fits to the two-level charge-carrier mobility model. d) Fluence-dependent charge-carrier recombination transients beyond 2.5 ps, i.e., following the initial ultrafast decay, measured after 3.1 eV pulsed excitation for $AgBiS_2$ NC thin films annealed at 150 °C. Solid lines represent fits to the charge-carrier recombination model described in Note S5 (Supporting Information). Open circles are experimental data, and solid lines represent fits to the two-level mobility model. e) Effective THz charge-carrier mobilities for $AgBiS_2$ NC thin films plotted as a function of annealing temperatures extracted from photoconductivity transients (see Note S3, Supporting Information). Dashed lines are guides to the eye, indicating the mobility increase with increasing annealing temperatures. In the inset, colored triangles indicate the ratio between localized and initial mobility for $AgBiS_2$ NC thin films as a function of the annealing temperature. f) Contour plot of the diffusion length as a function of charge-carrier mobility and lifetime, calculated at a nominal charge-carrier density of 10^{16} cm^{-3} (see details in Note S5, Supporting Information) The value for $AgBiS_2$ NC thin films annealed at 150 °C is indicated with a brown open triangle. Other reference values are obtained from the literature (PbSe,[56] $FA_{1-y}Cs_yPb(I_xCl_{1-x})_3$,[57] $NaBiS_2$,[20] Cu_2AgBiI_6,[29] $Cs_2AgBiBr_6$,[27] P3HT:PCBM[58]) and had been estimated by using a similar approach. To ensure comparability, all of the listed diffusion lengths were calculated from THz photoconductivity data.

Photoconductivity transients shown in Figure 2a further reveal an ultrafast initial decay and subsequent plateau for all of the studied $AgBiS_2$ NC thin films, independently of the annealing temperature. Crucially, similar behavior of the photoconductivity has been reported for several silver-bismuth and bismuth-based ABZ_2 semiconductors (e.g., $Cs_2AgBiBr_6$, Cu_2AgBiI_6, $NaBiS_2$, $Cu_{4x}(AgBi)_{1-x}I_4$)[20,27–30] and has been attributed to ultrafast charge-carrier localization occurring within the first picosecond after excitation. In these studies, the observed dynamics of the photoconductivity has been attributed to an initial formation of highly delocalized large polarons with high mobility, which subsequently transfer to a localized small-polaron state with significantly lower mobility. For the $AgBiS_2$ NC films investigated here, we also assign the observed dynamics to charge-carrier localization, given the lack of fluence dependence for this ultrafast decay and its persistence at low pump fluences (<30 μJ cm^{-2}), which rules out possible contributions from higher-order recombinations (Figure 2b; and Figure S8a–d, Supporting Information) over this time scale. As shown in Figure 2a, fits to our data based on the two-level mobility model developed by Wright, Buizza et al.[27,29] (described in the Note S4, Supporting Information) to describe an ultrafast charge-carrier mobility change

© 2023 The Authors. Advanced Materials published by Wiley-VCH GmbH

15214095, 2023, 48, Downloaded from https://onlinelibrary.wiley.com/doi/10.1002/adma.202305009 by Test, Wiley Online Library on [12/12/2023]. See the Terms and Conditions (https://onlinelibrary.wiley.com/terms-and-conditions) on Wiley Online Library for rules of use; OA articles are governed by the applicable Creative Commons License

arising from charge-carrier localization accurately reproduce the observed photoconductivity for all the studied $AgBiS_2$ NC thin films and therefore confirm our interpretation.

Both the initial charge-carrier mobilities and those of the subsequent localized state (μ_i and μ_{loc}) are found to increase consistently (Figure 2e) with increasing annealing temperature for $AgBiS_2$ NC thin films. While the mobility of the localized state, $\mu_{loc,}$ increases from 0.11 ± 0.05 cm^2 V^{-1} s^{-1} for the as-prepared thin films to 2.20 ± 0.10 cm^2 V^{-1} s^{-1} for the films annealed at 150 °C, the initial mobility μ_i increases from 0.43 ± 0.05 cm^2 V^{-1} s^{-1} for the as-prepared films to 2.70 ± 0.10 cm^2 V^{-1} s^{-1} for the films annealed at 150 °C. We note that although the mobilities follow a similar increasing trend with anneal temperature, importantly, the fraction of retained mobility after the localization process, $p = \mu_{loc}/\mu_i$, increases substantially from ≈25% to ≈80% (inset of Figure 2e; and Figure S10, Supporting Information) from the as-prepared film to that annealed at 150 °C. Notably, this "mobility retention" value is significantly higher than those previously reported for $Cs_2AgBiBr_6$ ($p \approx 30\%$),[27] Cu_2AgBiI_6 ($p \approx 45\%$),[29] and other semiconductors experiencing ultrafast charge-carrier localization.[20,59] Therefore, the impact of the charge-carrier localization process is largely mitigated and charge-carrier transport is increasingly preserved as the annealing temperature is increased and homogeneous CD is introduced in $AgBiS_2$ NC thin films. Our observations thus reveal the critical role of cation-disorder engineering for mitigating ultrafast charge-carrier localization in such materials.

We are further able to determine values for the charge-carrier diffusion length based on additional analysis of charge-carrier lifetimes in $AgBiS_2$ NC thin films. Following the initial localization process, charge carriers recombine over a sub-nanosecond time scale, as shown in Figure 2c. Through global fits to this fluence-dependent set of transients, we are able to extract the rates of monomolecular (k_1) and bimolecular (k_2) recombination rate constants, as detailed in Note S5 (Supporting Information). We note that the extracted value for the bimolecular rate constants for $AgBiS_2$ NC thin films in the range $k_2 \approx 2 - 5 \times 10^{-10}$ cm^{3}s^{-1} describing electron–hole band-to-band recombination is comparable to the values previously reported for other emerging semiconductors, e.g., $k_2 \approx 0.3 - 6 \times 10^{-10}$ cm^{3}s^{-1} for $Cu_{4x}(AgBi)_{1-x}I_4$[30] and $k_2 \approx 6.8 \times 10^{-10}$ cm^{3}s^{-1} for methylammonium lead iodide.[60] This finding is in apparent contrast with the stronger light–matter interaction observed for $AgBiS_2$, outlined by the particularly strong absorption coefficient value near the band edge (around 10^5 cm^{-1}, see Figure 1c). We note that according to the principle of detailed balance, a relation between the absorption coefficient and the bimolecular recombination rate would be expected according to the Shockley–van Roosbroeck equation.[61,62] Our observation of a bimolecular recombination coefficient for $AgBiS_2$ comparable to that of other emerging semiconductors showing significantly lower direct absorption coefficients could be explained by the weaker light–matter interaction of the localized state. We further used the extracted monomolecular and bimolecular recombination coefficients, and the charge-carrier mobility value for the localized state, $\mu_{loc,}$ to determine a charge-carrier diffusion length of $L_D \approx 50$ nm for $AgBiS_2$ NC films annealed at 150 °C (see Note S5 for details, Supporting Information). We note that diffusion length values reported here are based on THz photoconductivity measurements, which mainly probe short-range transport that is likely to fall within the nanocrystal boundaries.[50] This hypothesis is further confirmed by the increased backscattering observed in the photoconductivity spectra (Figure S7, Supporting Information) for thin films with larger L_D. As further discussed in Note S5 (Supporting Information), this complicates comparison with L_D values derived from techniques probing long-range conduction, such as space-charge-limited current, time-of-flight and photo-CELIV.[33,63] As such, the values we report here are thus reflective of the intrinsic semiconductor material quality and present an ideal scenario of conduction in the absence of boundary limitations. As shown in Figure 2e, such diffusion length values derived from THz photoconductivity measurements are significantly higher for the $AgBiS_2$ NCs examined here than for $NaBiS_2$[20] and organic semiconductors,[58] and close to those for other emerging metal halide semiconductors.[27,29,30] In conjunction with the enhanced absorption coefficients allowing for ultrathin light-absorber layers, our findings thus explain the recently reported exceptional performance of cation-disorder engineered $AgBiS_2$ NCs as active layers in solar cells.[22,32]

2.3. Cation Disorder and Charge-Carrier Localization in $AgBiS_2$ NC Thin Films

To understand how and why cation-disorder engineering can be used as an effective tool to suppress charge-carrier localization, we conducted temperature-dependent OPTP measurements on $AgBiS_2$ NC thin films annealed at 150 °C. As shown in **Figure 3**a for 4 and 295 K (and Figure S12 for further temperatures, Supporting Information) the initial ultrafast photoconductivity decay becomes even more prominent toward lower temperatures, and the subsequent decay accelerates. We are again able to fit such transients with the two-level mobility model, and find the resulting localization constant k_{loc} (Figure S13a, Supporting Information) to be mainly temperature independent, thus strongly supporting the hypothesis of a barrierless localization process.[27,29] We note that similar barrier-free self-trapping processes have been predicted by the theory developed by Holstein and Emin[64] to occur for the specific case of 2D semiconductors.[65] In contrast, for 3D semiconductors, a finite energy barrier is predicted to result in the coexistence of free carriers and polaron. We propose that the lower electronic dimensionality of silver-bismuth semiconductors (i.e., deviations from isotropic orbital connectivity of the band edges)[54,55] can yield barrier-free behavior even in structurally 3D semiconductors. On the other hand, the accelerated decay is captured by the increased recombination constant k_R at lower temperatures (Figure S13b, Supporting Information), which we attribute to increased contribution from direct electron–hole bimolecular recombination, as discussed in the Supporting Information.

In addition, we find different temperature dependencies for the extracted values for μ_i and μ_{loc} (Figure 3b), which indicates an alteration in the nature of charge carriers following the localization process. μ_{loc} decreases with decreasing temperature, whereas μ_i is found to increase when decreasing temperature from 295 to 50 K and to decrease again for $T < 50$ K. A power-law dependence $\mu \propto T^{\gamma}$ accurately describes the observed trends for extracted μ_i and μ_{loc}, and least-square fitting yields a negative-valued

© 2023 The Authors. Advanced Materials published by Wiley-VCH GmbH

15214095, 2023, 48, Downloaded from https://onlinelibrary.wiley.com/doi/10.1002/adma.202305009 by Test, Wiley Online Library on [12/12/2023]. See the Terms and Conditions (https://onlinelibrary.wiley.com/terms-and-conditions) on Wiley Online Library for rules of use; OA articles are governed by the applicable Creative Commons License

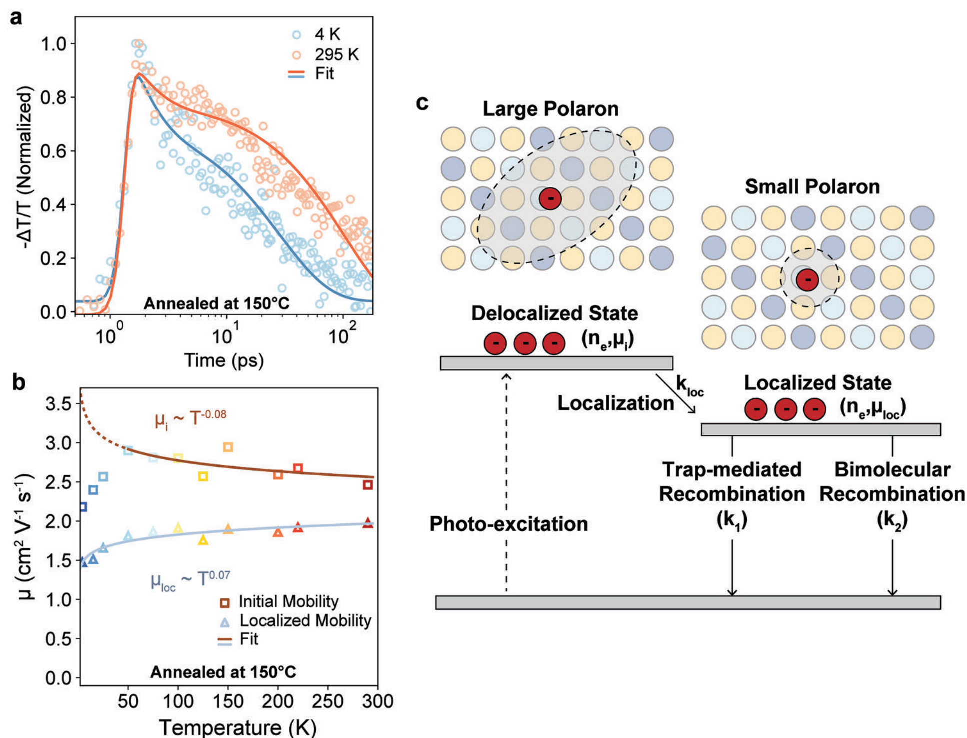

Figure 3. Temperature-dependent THz photoconductivity of charge carriers in $AgBiS_2$ NC films. a) Comparison between photoinduced THz conductivity transients measured at 295 K (orange) and at 4 K (blue) for $AgBiS_2$ NC thin film annealed 150 °C, after 3.1 eV pulsed excitation at a fluence of 29 μJ cm^{-2}. Solid lines represent fits to the two-level mobility model described by Equation (S9) (convoluted with a Gaussian instrumental response function) in the Supporting Information. b) Temperature-dependence of effective THz charge-carrier mobilities immediately following excitation, μ_i (squares), and after localization, μ_{loc} (triangles), for $AgBiS_2$ NC thin film annealed 150 °C, extracted from the analysis of photoconductivity presented in Note S3 (Supporting Information). Solid lines represent power-law fits to the experimental mobility values. Note that for μ_i the fit excludes points at $T < 50$ K, which significantly deviate from the trend, thus indicating a different scattering mechanism. c) Schematic illustration of the charge-carrier dynamics observed for $AgBiS_2$ NC thin films, according to the two-level mobility model. After the initial photoexcitation of charge carriers (dotted line) via pulsed laser excitation, a delocalized state is populated by a density n_c of charge carriers experiencing bandlike (large-polaron) transport with a mobility μ_i. These charge-carriers undergo a fast localization process, with rate k_{loc}. The population is then transferred to a localized small-polaron state, which experiences temperature-activated, hopping-like transport with mobility μ_{loc} and recombines either via monomolecular (e.g., trap-mediated) or bi-molecular (radiative electron–hole) recombination processes.

exponent $r \approx -0.08$ for μ_i in the range 295–50 K and a positive one of $r \approx 0.07$ for μ_{loc} over the full temperature range. The negative exponent observed for μ_i strongly indicates bandlike transport and weak electron–phonon interactions for initial photoexcitations in $AgBiS_2$ NC films, suggesting the initial presence of "large polarons".[66] On the other hand, the positive exponent observed after the ultrafast decay is indicative of strong electron–phonon coupling and reflects a temperature-activated "hopping" transport regime, typical of "small polarons".[67–69] Overall, our OPTP measurements thus indicate the presence of an ultrafast localization process in $AgBiS_2$, causing an ultrafast, barrierless transition between an initially-excited delocalized large-polaron state and a localized small polaronic state, similar to processes occurring in Cu_2AgBiI_6 and $Cs_2AgBiBr_6$.[27,29]

We comment briefly on the nature of the large polaron state initially created, noting that the power law dependence observed for mobility, with the negative exponent $r \approx -0.08$ over the temperature range 295–50 K, has an exponent significantly lower than those previously reported for conventional and emerging semiconductors, e.g., $r \approx -2.4$, -2.1, and -1.5 for Si, GaAs, and methylammonium lead iodide.[66,70,71] However, similarly low exponents were reported for Cu_2AgBiI_6 ($r \approx -0.33$) and $Cs_2AgBiBr_6$ ($r \approx -0.47$) and were assigned to the presence of multiple intrinsic and extrinsic contributions.[27,29] Several scattering processes and coupling interactions experienced by charge carriers generally contribute to determining the overall temperature dependence of charge-carrier mobility, e.g., polar (Fröhlich) interaction, acoustic deformation potential and piezoelectric coupling.[71,72] The presence of multiple scattering components is further confirmed by the decaying trend with lower temperatures observed for μ_i at $T < 50$ K. A similar behavior has been observed for GaAs and other III–V semiconductors and can be ascribed to ionized impurity scattering, which is increased at lower temperatures as the average thermal speed of charge carriers decreases and they spend more time near the ionized impurity.[72,73] We note that these experimental observations thus confirm recent calculations suggesting that in $AgBiS_2$, polar optical phonon scattering at higher temperatures, and ionized impurity scattering at lower temperatures, should determine charge-carrier mobilities.[74]

Finally, we discuss why cation disorder has such a substantial effect on the extent to which the charge-carrier mobility is suppressed following the initial localization process. As illustrated

© 2023 The Authors. Advanced Materials published by Wiley-VCH GmbH

schematically in Figure 3c, excitation initially results in the generation of a delocalized large-polaron state. This state subsequently collapses into a localized small-polaron state, described by the theory of Holstein and Emin.[67–69] The dramatic change of transport regime following ultrafast localization, i.e., the transition between large-polaron bandlike to small-polaron hopping transport, is key to understanding how cation engineering influences the remnant localized mobility retained by the small-polaron state, as a fraction of the initial mobility (inset of Figure 2d). We posit that the transition from a delocalized state to a localized state exacerbates the impact of the disordered electronic landscape, and in particular of the tail states, on charge-carrier transport. Although the ultrafast localization process yields reduced charge-carrier mobility, the resulting small polarons are in principle still itinerant. However, we note that the localization of the charge-carrier wave function will also influence its interaction with defects and disorder. Anderson localization theory explains how disordered and defective electronic landscapes can transform an itinerant state into a localized one.[75] Importantly, such Anderson localization is more energetically-favored for small polarons compared to large polarons. Here, even relatively minimal disorder can result in immobile small polaron states according to the Holstein–Anderson theory developed by Bronold and co-workers.[76,77] According to these models, strong electron–phonon interactions are expected to deepen potential wells arising from energetic disorder, thus increasing the severity of the localization for small polarons. Based on these considerations, we are thus able to explain why homogeneous CD present in $AgBiS_2$ NC films annealed at 150 °C leads to significantly enhanced remnant charge-carrier mobility, compared with as-prepared films exhibiting significant cation segregation and a highly disordered energetic landscape.

Overall, the interplay between charge-carrier transport and CD engineering is thus multifaceted. First, homogeneous disorder yields a more spatially-delocalized DOS and therefore generally increases the overall charge-carrier mobility in $AgBiS_2$. Second, the transition from a cation-segregated configuration to a homogeneous CD configuration significantly reduces the electronic disorder (visualized as absorption tails), and thus preserves a higher mobility especially for small-polaronic states formed in these materials, which are otherwise highly susceptible to Anderson localization effects.

3. Conclusions

In this work, we have demonstrated that cation engineering induces significant enhancement of charge-carrier mobilities and unveiled the interplay between charge-carrier localization and cation disorder in $AgBiS_2$ NC thin films. Through cation disorder engineering, we obtained charge-carrier mobilities up to 2.7 ± 0.1 $cm^2\ V^{-1}\ s^{-1}$ values, making this environmentally-friendly nanomaterial competitive with more established lead-containing photovoltaic materials such as PbSe NCs.[56] Our analysis of absorption spectra uncovered the role of homogeneous cation disorder in achieving a more electronically-ordered landscape. Furthermore, through room temperature and cryogenic OPTP measurements, we have demonstrated the presence of an ultrafast charge-carrier localization process, whose relevance for long-range transport in device applications has been demonstrated for other bismuth halides,[27,78] and unveiled its interaction with cation disorder in silver-bismuth semiconductors. On a more fundamental level, our work provides insights into the charge-carrier dynamics of polaronic materials and highlights the crucial role of an ordered electronic landscape (achieved here via homogeneous cation disorder) in achieving efficient small-polaron transport. Our findings demonstrate the enormous potential of cation-disorder engineering for enhancing the optoelectronic properties of emerging multinary semiconductors. Overall, such possibility of tuning and achieving efficient polaronic transport in multinary semiconductors offers exciting opportunities for substantial advances in photovoltaics, light-emitting, and thermoelectrics applications.

Supporting Information

Supporting Information is available from the Wiley Online Library or from the author.

Acknowledgements

L.M.H. and M.R. thank the Engineering and Physical Sciences Research Council for funding (EPSRC, Grant No.: EP/V010840/1). L.M.H. acknowledges support through a Hans Fischer Senior Fellowship from the Technical University of Munich's Institute for Advanced Study, funded by the German Excellence Initiative. G.K. acknowledges financial support from the European Research Council (ERC) under the European Union's Horizon 2020 research and innovation programme (Grant Agreement No. 725165), the Fundació Joan Ribas Araquistain (FJRA), the Fundació Privada Cellex, the program CERCA, and "Severo Ochoa" Center of Excellence CEX2019-000910-S—Funded by the Spanish State Research Agency. Y.W. acknowledges the support from the European Union's Horizon 2020 research and innovation programme under the Marie Skłodowska-Curie Grant Agreement No. 754558.

Conflict of Interest

The authors declare no conflict of interest.

Data Availability Statement

The data that support the findings of this study are available from the corresponding author upon reasonable request.

Keywords

cation disorder, chalcogenides, charge-carrier transport, photovoltaic materials, THz spectroscopy, ultrafast localization

Received: May 26, 2023
Revised: September 1, 2023
Published online: October 24, 2023

[1] S. K. Wallace, D. B. Mitzi, A. Walsh, *ACS Energy Lett.* **2017**, *2*, 776.
[2] S. Giraldo, Z. Jehl, M. Placidi, V. Izquierdo-Roca, A. Pérez-Rodríguez, E. Saucedo, *Adv. Mater.* **2019**, *31*, 1806692.

© 2023 The Authors. Advanced Materials published by Wiley-VCH GmbH

15214095, 2023, 48, Downloaded from https://onlinelibrary.wiley.com/doi/10.1002/adma.202305009 by Test, Wiley Online Library on [12/12/2023]. See the Terms and Conditions (https://onlinelibrary.wiley.com/terms-and-conditions) on Wiley Online Library for rules of use; OA articles are governed by the applicable Creative Commons License

[3] M. D. Regulacio, M.-Y. Han, *Acc. Chem. Res.* **2016**, *49*, 511.
[4] J. Jian, G. Jiang, R. van de Krol, B. Wei, H. Wang, *Nano Energy* **2018**, *51*, 457.
[5] S. Y. Tee, D. Ponsford, C. L. Lay, X. Wang, X. Wang, D. C. J. Neo, T. Wu, W. Thitsartarn, J. C. C. Yeo, G. Guan, T.-C. Lee, M.-Y. Han, *Adv. Sci.* **2022**, *9*, 2204624.
[6] S. Ortega, M. Ibáñez, Y. Liu, Y. Zhang, M. V. Kovalenko, D. Cadavid, A. Cabot, *Chem. Soc. Rev.* **2017**, *46*, 3510.
[7] K. Alberi, M. B. Nardelli, A. Zakutayev, L. Mitas, S. Curtarolo, A. Jain, M. Fornari, N. Marzari, I. Takeuchi, M. L. Green, M. Kanatzidis, M. F. Toney, S. Butenko, B. Meredig, S. Lany, U. Kattner, A. Davydov, E. S. Toberer, V. Stevanovic, A. Walsh, N.-G. Park, A. Aspuru-Guzik, D. P. Tabor, J. Nelson, J. Murphy, A. Setlur, J. Gregoire, H. Li, R. Xiao, A. Ludwig, et al., *J. Phys. D: Appl. Phys.* **2019**, *52*, 013001.
[8] L. L. Baranowski, P. Zawadzki, S. Lany, E. S. Toberer, A. Zakutayev, *Semicond. Sci. Technol.* **2016**, *31*, 123004.
[9] R. R. Schnepf, J. J. Cordell, M. B. Tellekamp, C. L. Melamed, A. L. Greenaway, A. Mis, G. L. Brennecka, S. Christensen, G. J. Tucker, E. S. Toberer, S. Lany, A. C. Tamboli, *ACS Energy Lett.* **2020**, *5*, 2027.
[10] Q. Tian, S. Liu, *J. Mater. Chem. A* **2020**, *8*, 24920.
[11] D. Shin, B. Saparov, D. B. Mitzi, *Adv. Energy Mater.* **2017**, *7*, 1602366.
[12] P. Zawadzki, A. Zakutayev, S. Lany, *Phys. Rev. Appl.* **2015**, *3*, 034007.
[13] J. J. Cordell, M. K. Miller, M. B. Tellekamp, A. Tamboli, G. J. Tucker, S. Lany, *Phys. Rev. Appl.* **2022**, *18*, 064030.
[14] G. Rey, G. Larramona, S. Bourdais, C. Choné, B. Delatouche, A. Jacob, G. Dennler, S. Siebentritt, *Sol. Energy Mater. Sol. Cells* **2018**, *179*, 142.
[15] T. Gokmen, O. Gunawan, T. K. Todorov, D. B. Mitzi, *Appl. Phys. Lett.* **2013**, *103*, 103506.
[16] S. Kim, J.-S. Park, A. Walsh, *ACS Energy Lett.* **2018**, *3*, 496.
[17] S. Lany, A. N. Fioretti, P. P. Zawadzki, L. T. Schelhas, E. S. Toberer, A. Zakutayev, A. C. Tamboli, *Phys. Rev. Mater.* **2017**, *1*, 035401.
[18] J. J. Cordell, G. J. Tucker, A. Tamboli, S. Lany, *APL Mater.* **2022**, *10*, 011112.
[19] W. Chen, D. Dahliah, G.-M. Rignanese, G. Hautier, *Energy Environ. Sci.* **2021**, *14*, 3567.
[20] Y.-T. Huang, S. R. Kavanagh, M. Righetto, M. Rusu, I. Levine, T. Unold, S. J. Zelewski, A. J. Sneyd, K. Zhang, L. Dai, A. J. Britton, J. Ye, J. Julin, M. Napari, Z. Zhang, J. Xiao, M. Laitinen, L. Torrente-Murciano, S. D. Stranks, A. Rao, L. M. Herz, D. O. Scanlon, A. Walsh, R. L. Z. Hoye, *Nat. Commun.* **2022**, *13*, 4960.
[21] F. Viñes, G. Konstantatos, F. Illas, *Phys. Chem. Chem. Phys.* **2017**, *19*, 27940.
[22] Y. Wang, S. R. Kavanagh, I. Burgués-Ceballos, A. Walsh, D. O. Scanlon, G. Konstantatos, *Nat. Photonics* **2022**, *16*, 235.
[23] F. Viñes, M. Bernechea, G. Konstantatos, F. Illas, *Phys. Rev. B* **2016**, *94*, 235203.
[24] S. N. Guin, K. Biswas, *Chem. Mater.* **2013**, *25*, 3225.
[25] F. Viñes, G. Konstantatos, F. M. Illas, *J. Phys. Chem. B* **2018**, *122*, 521.
[26] J. A. Steele, P. Puech, M. Keshavarz, R. Yang, S. Banerjee, E. Debroye, C. W. Kim, H. Yuan, N. H. Heo, J. Vanacken, A. Walsh, J. Hofkens, M. B. J. Roeffaers, *ACS Nano* **2018**, *12*, 8081.
[27] A. D. Wright, L. R. V. Buizza, K. J. Savill, G. Longo, H. J. Snaith, M. B. Johnston, L. M. Herz, *J. Phys. Chem. Lett.* **2021**, *12*, 3352.
[28] B. Wu, W. Ning, Q. Xu, M. Manjappa, M. Feng, S. Ye, J. Fu, S. Lie, T. Yin, F. Wang, T. W. Goh, P. C. Harikesh, Y. K. E. Tay, Z. X. Shen, F. Huang, R. Singh, G. Zhou, F. Gao, *Sci. Adv.* **2021**, *7*, eabd3160.
[29] L. R. V. Buizza, A. D. Wright, G. Longo, H. C. Sansom, C. Q. Xia, M. J. Rosseinsky, M. B. Johnston, H. J. Snaith, L. M. Herz, *ACS Energy Lett.* **2021**, *6*, 1729.
[30] L. R. V. Buizza, H. C. Sansom, A. D. Wright, A. M. Ulatowski, M. B. Johnston, H. J. Snaith, L. M. Herz, *Adv. Funct. Mater.* **2022**, *32*, 2108392.
[31] M. Bernechea, N. Cates, G. Xercavins, D. So, A. Stavrinadis, G. Konstantatos, *Nat. Photonics* **2016**, *10*, 521.
[32] I. Burgués-Ceballos, Y. Wang, M. Z. Akgul, G. Konstantatos, *Nano Energy* **2020**, *75*, 104961.
[33] Y. Wang, L. Peng, Z. Wang, G. Konstantatos, *Adv. Energy Mater.* **2022**, *12*, 2200700.
[34] A. BaQais, N. Tymińska, T. Le Bahers, K. Takanabe, *Chem. Mater.* **2019**, *31*, 3211.
[35] M. D. Sturge, *Phys. Rev.* **1962**, *127*, 768.
[36] O. Rubel, S. D. Baranovskii, K. Hantke, B. Kunert, W. W. Rühle, P. Thomas, K. Volz, W. Stolz, *Phys. Rev. B* **2006**, *73*, 233201.
[37] R. J. Potter, N. Balkan, *J. Phys.: Condens. Matter* **2004**, *16*, S3387.
[38] J. Mattheis, U. Rau, J. H. Werner, *J. Appl. Phys.* **2007**, *101*, 113519.
[39] W. M. Linhart, S. J. Zelewski, P. Scharoch, F. Dybała, R. Kudrawiec, *J. Mater. Chem. C* **2021**, *9*, 13733.
[40] P. K. Sarswat, M. L. Free, *Phys. B* **2012**, *407*, 108.
[41] M. Baleva, T. Georgiev, G. Lashkarev, *J. Phys.: Condens. Matter* **1990**, *2*, 2935.
[42] R. A. Laff, *J. Appl. Phys.* **1965**, *36*, 3324.
[43] J. Bhosale, A. K. Ramdas, A. Burger, A. Muñoz, A. H. Romero, M. Cardona, R. Lauck, R. K. Kremer, *Phys. Rev. B* **2012**, *86*, 195208.
[44] E. S. Parrott, T. Green, R. L. Milot, M. B. Johnston, H. J. Snaith, L. M. Herz, *Adv. Funct. Mater.* **2018**, *28*, 1802803.
[45] M. I. Dar, G. Jacopin, S. Meloni, A. Mattoni, N. Arora, A. Boziki, S. M. Zakeeruddin, U. Rothlisberger, M. Grätzel, *Sci. Adv. 2*, e1601156.
[46] L. D. Whalley, J. M. Skelton, J. M. Frost, A. Walsh, *Phys. Rev. B* **2016**, *94*, 220301.
[47] H. Kim, J. Hunger, E. Cánovas, M. Karakus, Z. Mics, M. Grechko, D. Turchinovich, S. H. Parekh, M. Bonn, *Nat. Commun.* **2017**, *8*, 687.
[48] S. Meloni, G. Palermo, N. Ashari-Astani, M. Grätzel, U. Rothlisberger, *J. Mater. Chem. A* **2016**, *4*, 15997.
[49] A. M. Ulatowski, L. M. Herz, M. B. Johnston, *J. Infrared Millim. Terahertz Waves* **2020**, *41*, 1431.
[50] S. G. Motti, F. Krieg, A. J. Ramadan, J. B. Patel, H. J. Snaith, M. V. Kovalenko, M. B. Johnston, L. M. Herz, *Adv. Funct. Mater.* **2020**, *30*, 1909904.
[51] H. Hempel, R. Eichberger, I. Repins, T. Unold, *Thin Solid Films* **2018**, *666*, 40.
[52] L. Q. Phuong, M. Okano, G. Yamashita, M. Nagai, M. Ashida, A. Nagaoka, K. Yoshino, Y. Kanemitsu, *Phys. Rev. B* **2015**, *92*, 115204.
[53] L. L. Baranowski, K. McLaughlin, P. Zawadzki, S. Lany, A. Norman, H. Hempel, R. Eichberger, T. Unold, E. S. Toberer, A. Zakutayev, *Phys. Rev. Appl.* **2015**, *4*, 044017.
[54] D. H. Fabini, R. Seshadri, M. G. Kanatzidis, *MRS Bull.* **2020**, *45*, 467.
[55] Z. Xiao, W. Meng, J. Wang, D. B. Mitzi, Y. Yan, *Mater. Horiz.* **2017**, *4*, 206.
[56] G. W. Guglietta, B. T. Diroll, E. A. Gaulding, J. L. Fordham, S. Li, C. B. Murray, J. B. Baxter, *ACS Nano* **2015**, *9*, 1820.
[57] K. B. Lohmann, S. G. Motti, R. D. J. Oliver, A. J. Ramadan, H. C. Sansom, Q. Yuan, K. A. Elmestekawy, J. B. Patel, J. M. Ball, L. M. Herz, H. J. Snaith, M. B. Johnston, *ACS Energy Lett.* **2022**, *7*, 1903.
[58] P. Parkinson, J. Lloyd-Hughes, M. B. Johnston, L. M. Herz, *Phys. Rev. B* **2008**, *78*, 115321.
[59] R. Hooijer, A. Weis, A. Biewald, M. T. Sirtl, J. Malburg, R. Holfeuer, S. Thamm, A. A. Y. Amin, M. Righetto, A. Hartschuh, L. M. Herz, T. Bein, *Adv. Opt. Mater.* **2022**, *10*, 2200354.
[60] T. W. Crothers, R. L. Milot, J. B. Patel, E. S. Parrott, J. Schlipf, P. Müller-Buschbaum, M. B. Johnston, L. M. Herz, *Nano Lett.* **2017**, *17*, 5782.
[61] W. van Roosbroeck, W. Shockley, *Phys. Rev.* **1954**, *94*, 1558.
[62] C. L. Davies, M. R. Filip, J. B. Patel, T. W. Crothers, C. Verdi, A. D. Wright, R. L. Milot, F. Giustino, M. B. Johnston, L. M. Herz, *Nat. Commun.* **2018**, *9*, 293.

© 2023 The Authors. Advanced Materials published by Wiley-VCH GmbH

15214095, 2023, 48, Downloaded from https://onlinelibrary.wiley.com/doi/10.1002/adma.202305009 by Test, Wiley Online Library on [12/12/2023]. See the Terms and Conditions (https://onlinelibrary.wiley.com/terms-and-conditions) on Wiley Online Library for rules of use; OA articles are governed by the applicable Creative Commons License

[63] S. L. Diedenhofen, M. Bernechea, K. M. Felter, F. C. Grozema, L. D. A. Siebbeles, *Sol. RRL* **2019**, *3*, 1900075.
[64] D. Emin, T. Holstein, *Phys. Rev. Lett.* **1976**, *36*, 323.
[65] V. V. Kabanov, O. Y. Mashtakov, *Phys. Rev. B* **1993**, *47*, 6060.
[66] P. Y. Yu, M. Cardona, in *Fundamentals of Semiconductors: Physics and Materials Properties*, (Eds: P. Y. Yu, M. Cardona), Springer, Berlin **2010**, pp. 203–241.
[67] T. Holstein, *Ann. Phys.* **1959**, *8*, 343.
[68] D. Emin, *Phys. Rev. B* **1971**, *4*, 3639.
[69] J. Schnakenberg, *Z. Phys. A* **1968**, *208*, 165.
[70] L. M. Herz, *ACS Energy Lett.* **2017**, *2*, 1539.
[71] B. Van Zeghbroeck, *Principles of Semiconductor Devices and Heterojunctions*, Prentice Hall PTR, Hoboken, NJ **2007**.
[72] C. M. Wolfe, G. E. Stillman, W. T. Lindley, *J. Appl. Phys.* **1970**, *41*, 3088.
[73] F. J. Blatt, *J. Phys. Chem. Solids* **1957**, *1*, 262.
[74] T. Deng, J. Recatala-Gomez, M. Ohnishi, D. V. M. Repaka, P. Kumar, A. Suwardi, A. Abutaha, I. Nandhakumar, K. Biswas, M. B. Sullivan, G. Wu, J. Shiomi, S.-W. Yang, *Mater. Horiz.* **2021**, *8*, 2463.
[75] P. W. Anderson, *Phys. Rev.* **1958**, *109*, 1492.
[76] F. X. Bronold, H. Fehske, *Phys. Rev. B* **2002**, *66*, 073102.
[77] F. X. Bronold, A. Alvermann, H. Fehske, *Philos. Mag.* **2004**, *84*, 673.
[78] Z. Li, S. P. Senanayak, L. Dai, G. Kusch, R. Shivanna, Y. Zhang, D. Pradhan, J. Ye, Y.-T. Huang, H. Sirringhaus, R. A. Oliver, N. C. Greenham, R. H. Friend, R. L. Z. Hoye, *Adv. Funct. Mater.* **2021**, *31*, 2104981.

© 2023 The Authors. Advanced Materials published by Wiley-VCH GmbH

15214095, 2023, 48, Downloaded from https://onlinelibrary.wiley.com/doi/10.1002/adma.202305009 by Test, Wiley Online Library on [12/12/2023]. See the Terms and Conditions (https://onlinelibrary.wiley.com/terms-and-conditions) on Wiley Online Library for rules of use; OA articles are governed by the applicable Creative Commons License